Electronic Supplementary Information (ESI) for

Surface polarization of BiOI to boost the photoelectrochemical signal transduction for high performance bioassays

Mengmeng Gu,[a] Yuting Gong,[a] Xiuming Wu,[a] Yuming Dong,[a] and Guang-Li Wang*[a,b]

[a]Key Laboratory of Synthetic and Biological Colloids (Ministry of Education), School of Chemical and Material Engineering, Jiangnan University, Wuxi 214122, China

[b]Shandong Key Laboratory of Biochemical Analysis, College of Chemistry and Molecular Engineering, Qingdao University of Science and Technology, Qingdao 266042, China

*Corresponding author: Guang-Li Wang

*E-mail: glwang@jiangnan.edu.cn

Experimental Section

Reagents. The indium tin oxide (ITO) slices were purchased from China Southern Glass Holding Co., Ltd. (Shenzhen, China). Bismuth nitrate ($Bi(NO_3)_3 \cdot 5H_2O$), potassium iodide (KI), ethanol (EtOH), ethylene glycol (EG), glycerol (GLY), and doxorubicin (Dox) were all obtained from Sinopharm Chemical Reagent Co., Ltd. (Shanghai, China). The Mucin 1 (MUC1) protein was purchased from Saihongrui Biotechnology Co., Ltd. (Nanjing, China). All oligonucleotides (HPLC-purified) and the microRNA-122 (miR-122) were acquired from Sangon Biotechnology Co., Ltd. (Shanghai, China) and their corresponding sequences are listed in Table S1.

Table S1. Oligonucleotide Sequences Used in This Work

Name	Sequence (3′ to 5′)
Sequences used for probing miR-122	
miR-122	UGG AGU GUG ACA AUG GUG UUU G
Hairpin probe	CGA CGT CGG CTC T**AA CAC CAT TGT CAC ACT C**TA GAG CCG ACG TCG
Help probe (HP)	TCA TTC TAG AGT GTG ACA ATG GTG TTA GAA TGA
Sequences used for probing MUC1 protein	
Aptamer probe	AAT CTG **GCA GTT GAT CCT TTG GAT ACC CTG G**
Auxiliary probe	CC**A GGG TAA TAA CAG ATT**
Hairpin probe	CGA CGT GCC G**AA TCT GTT ATT ACC CT**C ATT CGG CAC GTC G
Help probe (HP′)	GTG AAT GAG GGT AAT AAC AGA TTC AC

Note: In the hairpin probes, the bold parts represent the recognition sites of miR-122 or the sequences complementary to the auxiliary probe, respectively; while the underlined parts represent the sequences complementary to the help probes (HP or HP′), respectively. In the aptamer probe, the bold parts represent the binding sites of MUC1 protein, and the underlined parts represent the sequences complementary to the auxiliary probe.

Apparatus. PEC measurements were conducted with a homemade PEC system including a LED lamp (λ=410–420 nm) as the illumination source (Tianjin Deshang Technology Co., Ltd., China) and a CHI 800C electrochemical workstation (CH Instruments, China) for the photocurrent record. The bismuth oxyiodides modified ITO slices, the Pt wire, and the saturated Ag/AgCl were employed as the working, counter and reference electrodes, respectively. Field emission scanning electron microscopy (FE-SEM) images were acquired by a Hitachi S-4800 scanning electron microscope (Hitachi, Japan). Transmission electron microscopy (TEM) images were obtained by a JEM-2100 Plus transmission electron microscope (Hitachi, Japan). X-ray photoelectron spectroscopy (XPS) was obtained from an Axis supra spectrometer (Kratos, UK). The phase structure of different bismuth oxyiodides were observed with the X-ray diffraction (XRD) on an X'Pert Philips materials research diffractometer (Bruker AXS, Germany). The Raman spectra were

conducted on an InVia Raman microscope spectrometer (Renishaw, UK). Fourier transform infrared (FT-IR) spectra were acquired from a FALA-2000104 spectrometer (Boman, Canada). The absorption spectra of the samples were recorded on a UV-vis-NIR-3600 spectrophotometer (Shimadzu, Japan). The fluorescence spectra were acquired with a Cary Eclipse fluorescence spectrophotometer (Varian Co. Ltd., USA). Thermogravimetry analysis (TGA) was conducted on a Q5000IR TGA analyzer (Mettler Toledo, Switzerland). Surface photovoltage (SPV) spectroscopy was acquired with a PL-SPS1000 surface photovoltage spectrometer (Zolix, China). Nitrogen adsorption and desorption isotherm curves were recorded by an ASAP 2460 surface area and porosity analyzer (Micromeritics, USA).

Hydrothermal Synthesis of Bismuth Oxyiodides with Different Degrees of Surface Hydroxylation. The bismuth oxyiodides were synthesized on the basis of a hydrothermal method. To synthesize bismuth oxyiodides with different degrees of surface hydroxylation, different alcohols, including ethanol (EtOH), ethylene (EG) and glycol glycerol (GLY), all at the volume of 38.0 mL were used for dissolving 0.3881 g of $Bi(NO_3)_3{\cdot}5H_2O$. At the same time, 0.1328 g of KI was dissolved in 2.0 mL of distilled water under continue stirring until the solution became clear and transparent. In the following, the above 2.0 mL of KI solution was slowly added to the above $Bi(NO_3)_3{\cdot}5H_2O$ solution under continuous stirring. Following that, the above reaction mixtures were transferred into reaction vessels and heated for 12 h at 130 °C. After naturally cooling to room temperature, the products were washed thoroughly with ethanol and distilled water, then dried at 60 °C for subsequent use.

Fabrication of the Bismuth Oxyiodides Modified ITO Electrodes. The as-obtained bismuth oxyiodides were utilized for modify the pretreated ITO electrodes that were treated[1] referring to our previous report. To deposit bismuth oxyiodides onto the ITO electrodes, a 30 μL of the bismuth oxyiodides' solution (prepared by dissolving the solid bismuth oxyiodides in water under ultrasonication to attain a concentration of 1.0 mg/mL) were dropped onto the ITO electrodes′ surface and dried in air.

PEC Detection of miR-122 and MUC1 Protein. For the experiment of sensing miR-122, the hairpin probe (20.0 μM, 30 μL) and Dox (45.0 μM, 40 μL) were mixed in 10.0 mM of Tris−HCl buffer (130 μL, pH 7.4, 1.0 mM $MgCl_2$) and incubated at 37 ℃ for 30 min to form the Dox intercalated hairpin probe (named as DIH); and then, a 20 μL of different concentrations of miR-122 and 20 μL of the help probe (HP, 40.0 μM) were sequentially added to the above solution and incubated at 37 ℃ for 2 h. Finally, the reaction mixture was used for further PEC analysis at the working potential of –0.1 V (*vs*. saturated Ag/AgCl).

For the experiment of sensing MUC1 protein, the hairpin probe (45.0 μM, 10 μL) and Dox (135.0 μM, 10 μL) were mixed with 10.0 mM Tris−HCl buffer (130 μL, pH 7.4, 1.0 mM $MgCl_2$) at 37 ℃

for 30 min to form the Dox intercalated hairpin probe (named as DIH′). At the same time, the MUC1 aptamer probe (20.0 μM, 20 μL) and the auxiliary probe (20.0 μM, 20 μL) were mixed in 10.0 mM of Tris−HCl (140 μL, pH 7.4, 1.0 mM $MgCl_2$) at 37 ℃ for 30 min, followed by the addition of various concentrations of MUC1 (20 μL) and was incubated for another 30 min. In the following, the above two reaction solutions were mixed with the help probe (HP′) (22.5 μM, 20 μL) and incubated for 2 h, which solution was intended for further PEC analysis at the working potential of –0.1 V (*vs*. saturated Ag/AgCl).

Polyacrylamide Gel Electrophoresis (PAGE) Analysis. Products were analyzed using a 15% polyacrylamide gel in TBE buffer (89 mM Tris-boric acid, pH = 8.0). All analytes were at a concentration of 5.0 μM, and 7.5 μL of the different analytes were mixed with 2.5 μL of loading buffer for sample loading. The assays were carried out at 90 V for 100 min. Afterwards, the obtained gels were stained with GelRed for 20 min and imaged by a Gel Doc XR+Imaging Analysis System (BIO-RAD, USA).

Determination of miR-122 and MUC1 Protein from the MCF-7 Cell Lysates. The MCF-7 cells were cultivated in Dulbecco′s Modified Eagle Medium (DMEM) comprising 10% fetal bovine serum (FBS), 100.0 U/mL penicillin, and 100.0 U/mL streptomycin in 5% CO_2 at 37 ^{o}C.[2] The total RNA and total protein used for the real sample to detect the content of miR-122 and MUC1 protein were extracted from MCF-7 cells using trizol reagent according to previously report.[3] The acquired cellular extracts were collected and stored at –20 °C for further use.

Supplementary Results

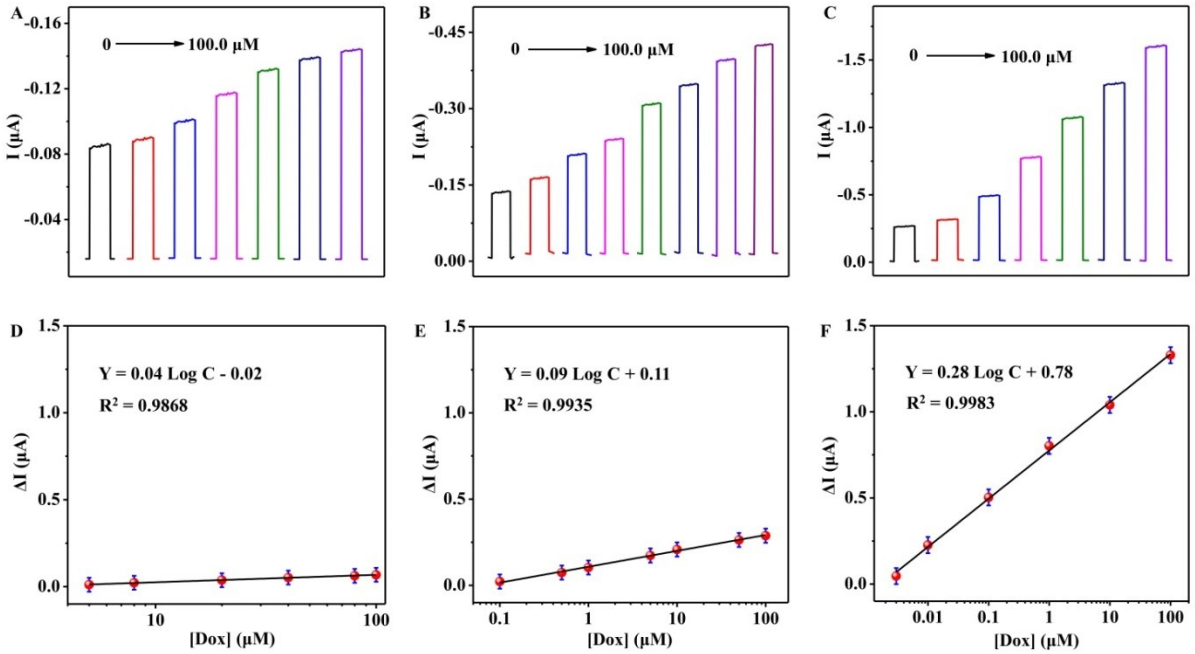

Figure S1. Photocurrent responses of (A) Bi (EtOH), (B) Bi (EG), and (C) Bi (GLY) modified electrodes to different concentrations of Dox. (D), (E), and (F) are the corresponding calibration curves.

As shown in Figure S1, the photocurrent signal increments for Bi (EtOH), Bi (EG), and Bi (GLY) are linearly related to the Dox concentrations within the ranges of 5.0–100, 0.1–100, and 0.003–100 μM, respectively. While the detection limits acquired by the PEC responses of Bi (EtOH), Bi (EG), and Bi (GLY) electrodes for Dox are 1.67 μM, 30 nM, and 1.0 nM (S/N=3, i.e. 3σ, where 3σ is the standard deviation from the 12 blank assays[4]), respectively.

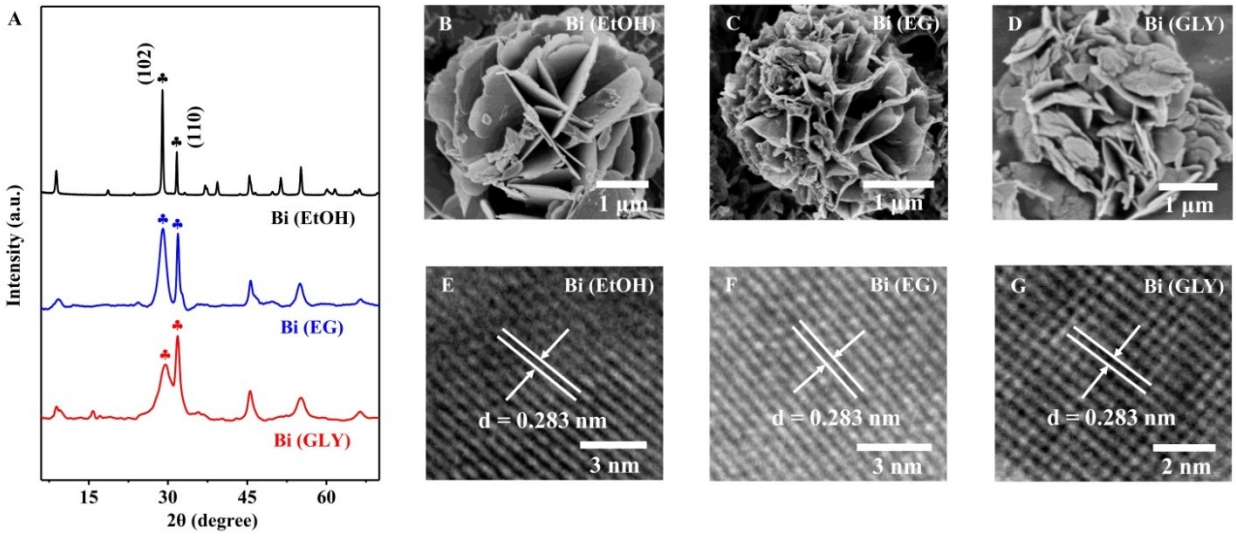

Figure S2. (A) XRD patterns of different bismuth oxyiodides. SEM and HRTEM images of (B, E) Bi (EtOH), (C, F) Bi (EG), and (D, G) Bi (GLY).

Apparently, all the diffraction peaks of these three products in the XRD patterns (Figure S2A) can correspond well with the tetragonal phase of BiOI (JCPDS no. 10-0445) with crystal lattice constants of $a = b = 3.994$ Å, and $c = 9.149$ Å. As noticed, the intensity ratios of the two diffraction peaks of $I_{\{110\}}/I_{\{102\}}$ increase progressively for Bi (EtOH), Bi (EG), and Bi (GLY), demonstrating that the Bi (GLY) is more inclined to grow along the {110} facet. This might be due to the fact that the growth rate of nanocrystal facets relies on the adsorption of solvents on the surface, which induces changes in crystals' specific surface free energy and the resultant crystal growth form.[5] Besides, the diffraction peaks widen gradually for Bi (EtOH), Bi (EG), and Bi (GLY), which may be caused by the reconstruction of surface structure of BiOI.[6] The SEM images show that all samples demonstrate similar flower–like hierarchical architectures assembled from nanosheets (Figure S2B-D), indicating that the bismuth oxyiodides synthesized in different solvents have no obvious variation in morphology. The HRTEM images (Figure S2E-G) disclose the heightened crystalline nature of all three samples, and the clearly visualized lattice fringes with lattice spacing of 0.283 nm corresponding to the {110} facet, indicating that there is no apparent crystal plane difference for all the synthesized bismuth oxyiodides.

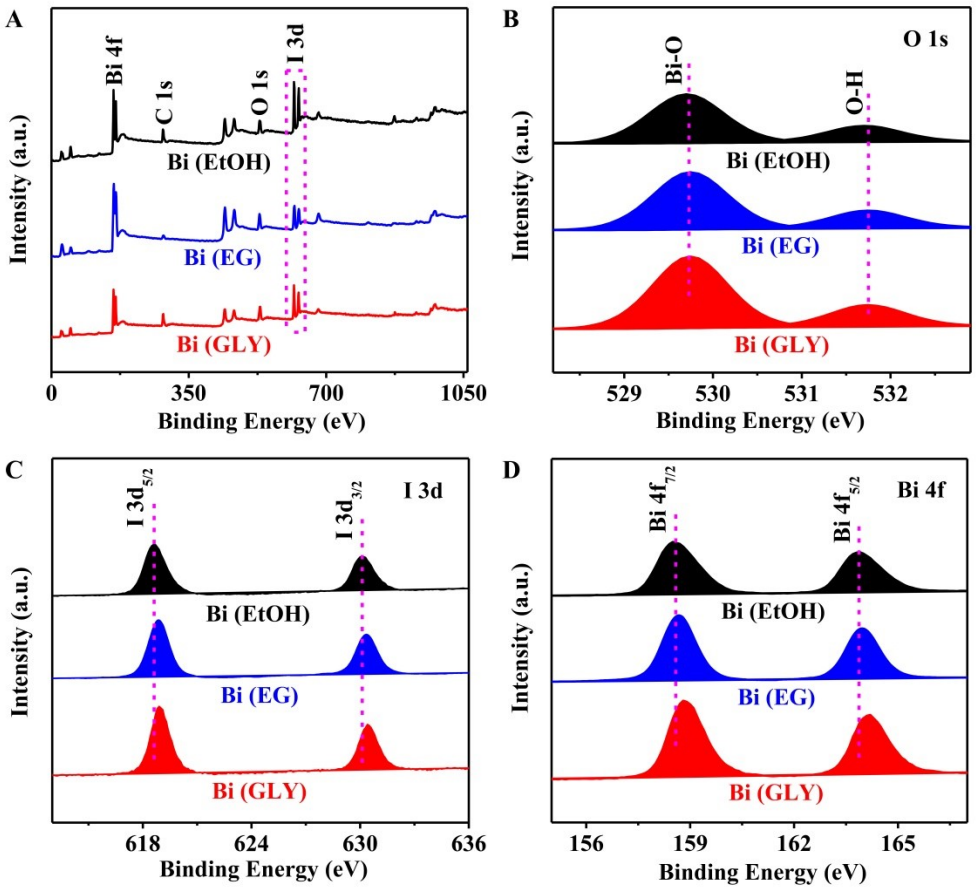

Figure S3. (A) Survey XPS spectra, (B) O 1s, (C) I 3d, and (D) Bi 4f high-resolution XPS spectra of different bismuth oxyiodides.

Figure S3A describes the survey XPS spectra of all the synthesized bismuth oxyiodides with the

associated elements of Bi, C, O, and I. In the XPS spectra of the oxygen core level (shown in Figure S3B), the major peaks at 529.7 and 531.7 eV are correlated with Bi-O and O-H bonds, respectively. It is apparent that the intensities of these two O-related peaks, indicators of the O-H quantity, are higher for Bi (GLY) than that of Bi (EtOH) and Bi (EG), validating the presence of more hydroxyl groups on the surface of Bi (GLY). In the I 3d spectra (Figure S3C), the peaks of I $3d_{5/2}$ and $3d_{3/2}$ in Bi (EtOH) and Bi (EG) are at 618.6, 630.0 eV, and at 618.7, 630.2 eV, respectively, while these peaks for Bi (GLY) slightly shift to higher energies at 618.9 and 630.4 eV. Similarly, a slight shift to higher energies of 158.9 and 164.2 eV can also be seen for Bi $4f_{7/2}$ and Bi $4f_{5/2}$ when compared with that of Bi (EtOH) (at 158.6 and 163.9 eV) and Bi (EG) (at 158.7 and 164.0 eV) (Figure S3D), hinting that the I–Bi bonds are also slightly changed due to the presence of different amounts of surface hydroxyl groups on bismuth oxyiodides.

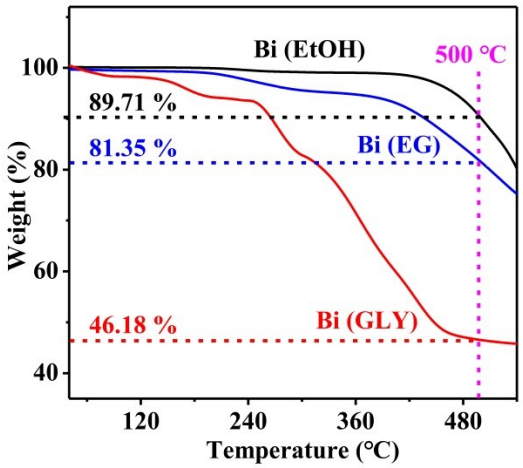

Figure S4. TGA analysis of different bismuth oxyiodides.

As known, TGA is typically used to express the gross weight loss of physisorbed and chemically−bound water, and the chemically−bound water is an indicator of surface hydroxyl groups, which can be obtained by deducting the physisorbed water from the gross mass loss.[7] The TGA analysis was executed and sheds light on the mass losses from 40 to 500 °C (Figure S4). The mass loss below 60 °C is attributable to the removal of physisorbed water, and the loss from 60 to 500 °C is considered to be the elimination of chemically-bound water. The losses of physisorbed water (below 60 °C) for all samples are very small, and the Bi (GLY) demonstrates the most dramatic chemically−bound water loss of mass (ca. 53.82 %) than that of Bi (EtOH) (ca. 10.29 %) and Bi (EG) (ca. 18.65 %), confirming increased amount of surface hydroxyl groups present on Bi (GLY).

We calculated the quantity of -OH by the Formula S1: $OH/nm^2 = [(OH/nm^2)^{T_2} \times SSA \times wt_{T_2} + 2N_A\ (wt_{T_1} - wt_{T_2})/MW_{H_2O})]/(SSA \times wt_{T_1}/\alpha)$,[7,8] where wt_{T_i} is the sample weight at the respective temperature, N_A is Avogadro's constant, MW_{H_2O} is the molecular weight of H_2O, α is calibration factor, and SSA is specific surface area. The value of α is 0.625. The SSA is obtained from nitrogen

adsorption and desorption isotherm curve at 77 K (Figure S5), and the SSAs of Bi (EtOH), Bi (EG) and Bi (GLY) are 13.4, 28.5 and 46.6 m^2/g, respectively. Finally, we derive the -OH quantities on the surface of Bi (EtOH), Bi (EG), and Bi (GLY) as 1.62, 2.15, and 4.61 OH/nm^2 respectively.

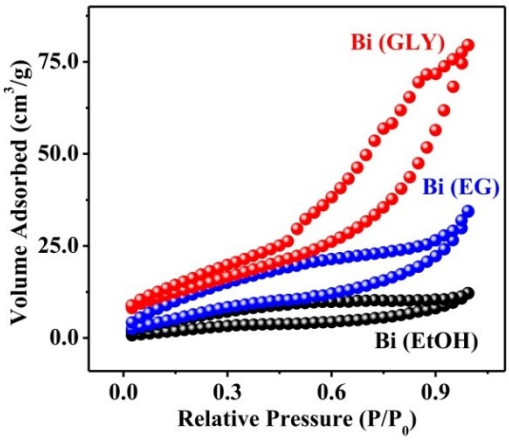

Figure S5. Nitrogen adsorption and desorption isotherm curves of different bismuth oxyiodides at 77 K.

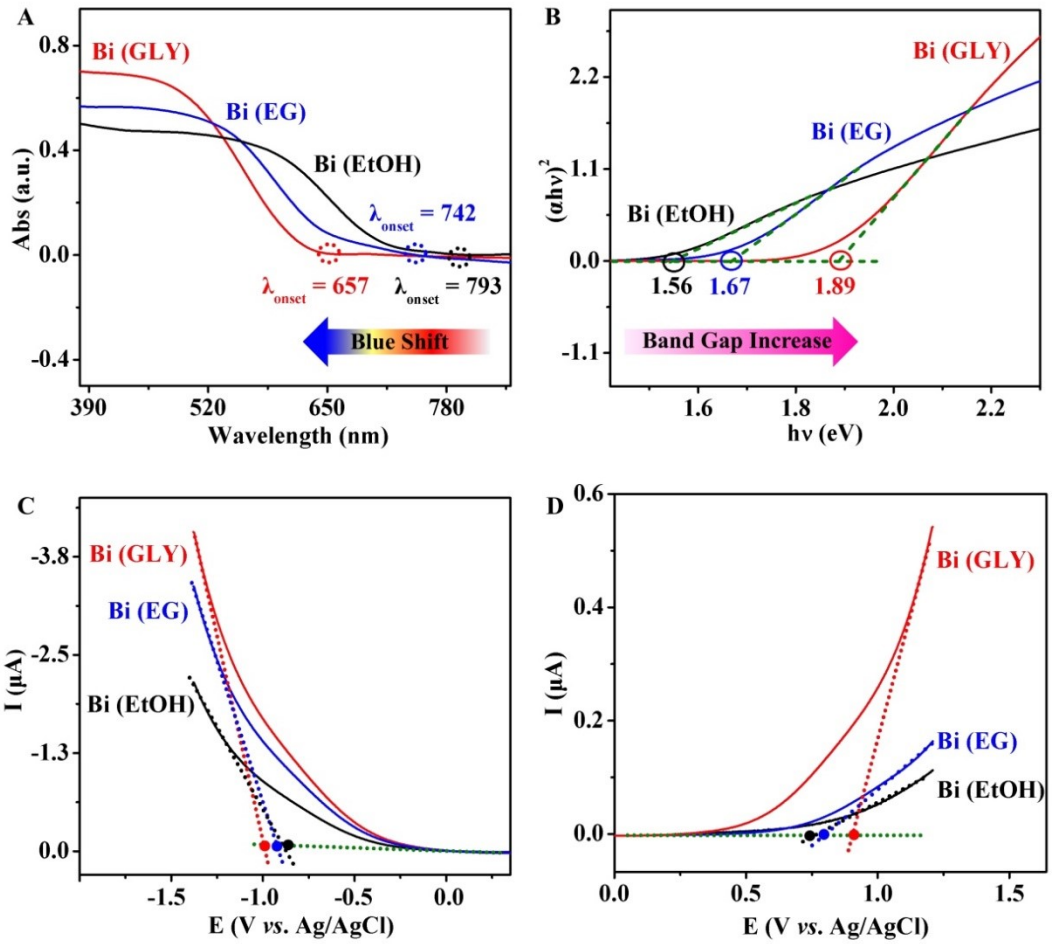

Figure S6. (A) UV-Vis-DRS spectra, (B) Tauc plots of $(\alpha h\nu)^2$ versus $h\nu$ for confirming the energy band gaps of different bismuth oxyiodides. (C) Cathodic and (D) anodic linear voltammetry scans for measuring the CB and VB edges of the bismuth oxyiodides. Experiments were performed in deaerated 0.2 M Na_2SO_4 solution.

The gradual increase in absorbance intensity in the range of 390-500 nm from Bi (EtOH), Bi (EG) to Bi (GLY) (Figure S6A) is mainly due to the difference in surface structure caused by different degrees of surface hydroxylation.[9] And the enhanced absorption leads to the generation of more charge carriers, thereby producing a higher photocurrent for BiOI (GLY) when in the absence of Dox (Figure 1A).

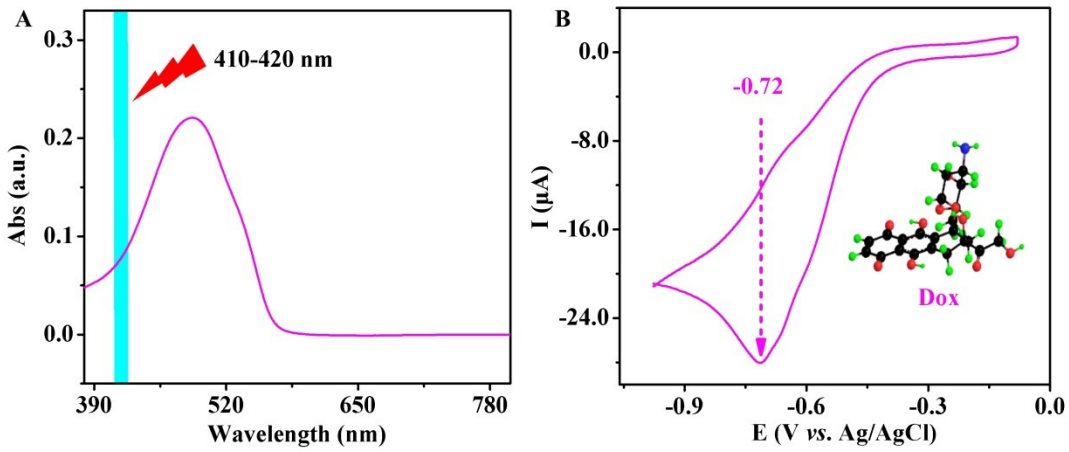

Figure S7. (A) UV-Vis absorption spectrum of Dox (10.0 μM) in 0.1 M Tris−HCl solution (pH = 7.4). (B) Cyclic voltammogram for measuring the reduction potential of Dox. The experiment was performed in 0.1 M Tris−HCl solution (pH = 7.4).

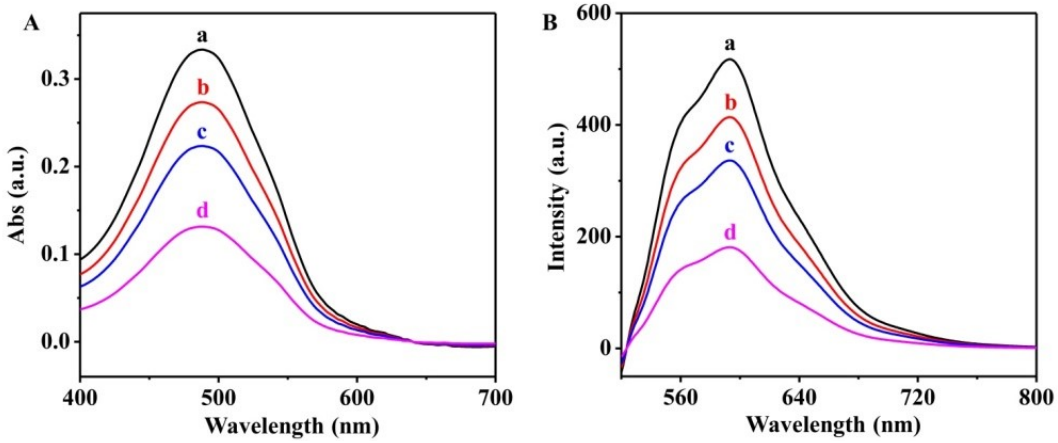

Figure S8. The absorption (A) and fluorescence (B) spectra of Dox (60.0 μM) before (a) and after incubated with the Bi (EtOH) (b), Bi (EG) (c), and Bi (GLY) (d) modified electrodes under irradiation with the LED light in the 410-420 nm band.

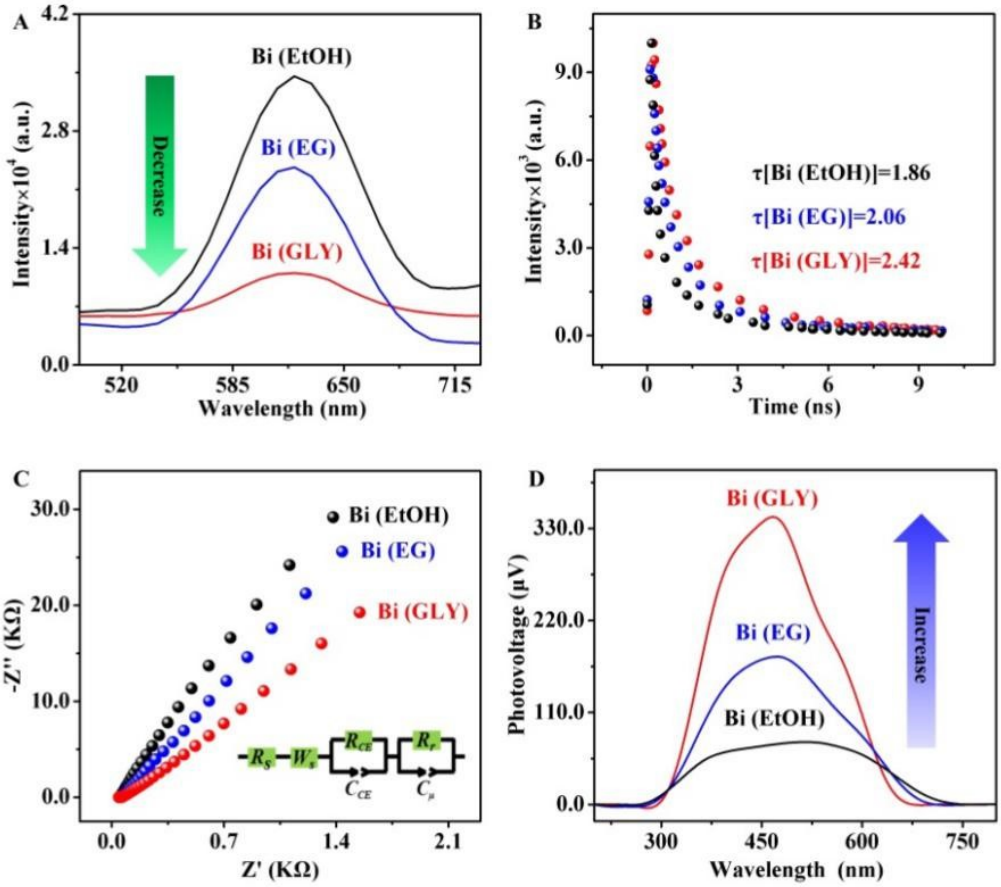

Figure S9. (A) PL, (B) TRPL, (C) EIS Nyquist diagram (experiments were performed in the 0.1 M Tris−HCl solution (pH = 7.4) from 100.0 kHz to 0.1 Hz), and (D) SPV spectra of different bismuth oxyiodides.

For the PL spectra, the minimum quantum yield for radiative excitons can be interpreted as the reinforced charge carrier separation efficiency.[10] As can be seen, a distinct emission maximum is observable at around 621 nm for all samples, but the Bi (GLY) manifests the lowest PL intensity (Figure S9A). All the TRPL decay curves were fitted with the double exponential decay model, as presented in Figure S9B and Table S2. The origin of fast decay component (τ_1) can be credited to non-radiative decay, while long decay component (τ_2) corresponds to the radiative recombination.[11] The lifetimes of both components increase gradually for Bi (EtOH), Bi (EG), and Bi (GLY): The fast decay components are 0.29, 0.36, and 0.49 ns, while the long decay components are 2.37, 2.94, and 3.47 ns, respectively. The average lifetimes for Bi (EtOH), Bi (EG), and Bi (GLY) are calculated as 1.86, 2.06, and 2.42 ns, respectively. The electrochemical impedance spectroscopy (EIS) technique (Figure S9C) was exploited to elaborate the charge-transfer resistances of different samples, which data were fitted with the equivalent circuit model exhibited in the inset of Figure S9C utilizing finite length Warburg-short circuit terminus (Ws) to clarify the electron transport (R_t) property. The smaller R_t, the higher charge transfer efficiency. The Bi (GLY) exhibits much smaller R_t (90.8 Ω) than that of the Bi (EtOH) (108.8 Ω) and Bi (EG) (95.2 Ω). The signal of SPV is ascribed to the variations in surface potential barriers before and after illumination, which can

furnish a swift and intuitive exploration of the carrier separation process.[12] Obviously, the SPV intensity is gradually enhanced from Bi (EtOH), Bi (EG) to Bi (GLY) (Figure S9D). In principle, the intensity of SPV is dictated by the velocity of charge carrier generation and recombination, and reinforced SPV signal manifests enhanced separation efficiency.

Table S2. Summary of the Lifetimes of Carriers for Different Bismuth Oxyiodides.

Sample	B_1	B_2	τ_1 (ns)	τ_2 (ns)	χ^2	τ_{avg} (ns)
Bi (EtOH)	4832.09	1829.32	0.29	2.37	1.13	1.86
Bi (EG)	5219.87	1237.53	0.36	2.94	1.41	2.06
Bi (GLY)	6436.92	1659.87	0.49	3.47	1.26	2.42

Fitting model: $R(\tau) = B_1e^{(-\tau/\tau_1)} + B_2e^{(-\tau/\tau_2)}$. Average fluorescence lifetime (τ_{avg}) calculation equation: $\tau_{avg} = (B_1\tau_1^2 + B_2\tau_2^2)/(B_1\tau_1 + B_2\tau_2)$, the τ_1 and τ_2 represent decay times, while the B_1 and B_2 are relative weights.

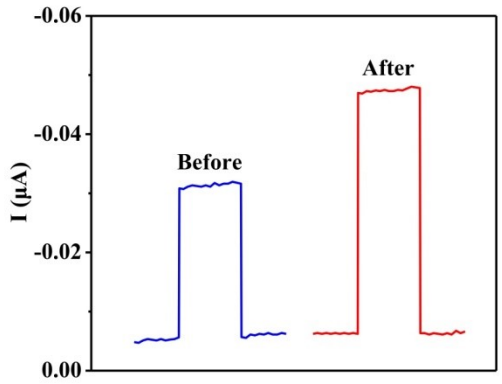

Figure S10. Photocurrent responses of dehydroxylated Bi (GLY) modified electrode before and after addition of 0.1 mM Dox in 0.1 M Tris−HCl solution (pH = 7.4) with –0.1 V (*vs*. Ag/AgCl) applied potential.

The surface hydroxyl groups of Bi (GLY) may be weakened by the calcination treatment.[13] The Bi (GLY) was calcined at 500 °C for 2 h, and then subjected the obtained dehydroxylated Bi (GLY) to PEC experiments. The experimental results (Figure S10) demonstrated that the photocurrent enhancement of dehydroxylated Bi (GLY) by Dox was significantly weakened, thus confirming the effect of surface hydroxylation induced polarization for promoting the PEC communication of Bi (GLY) with Dox.

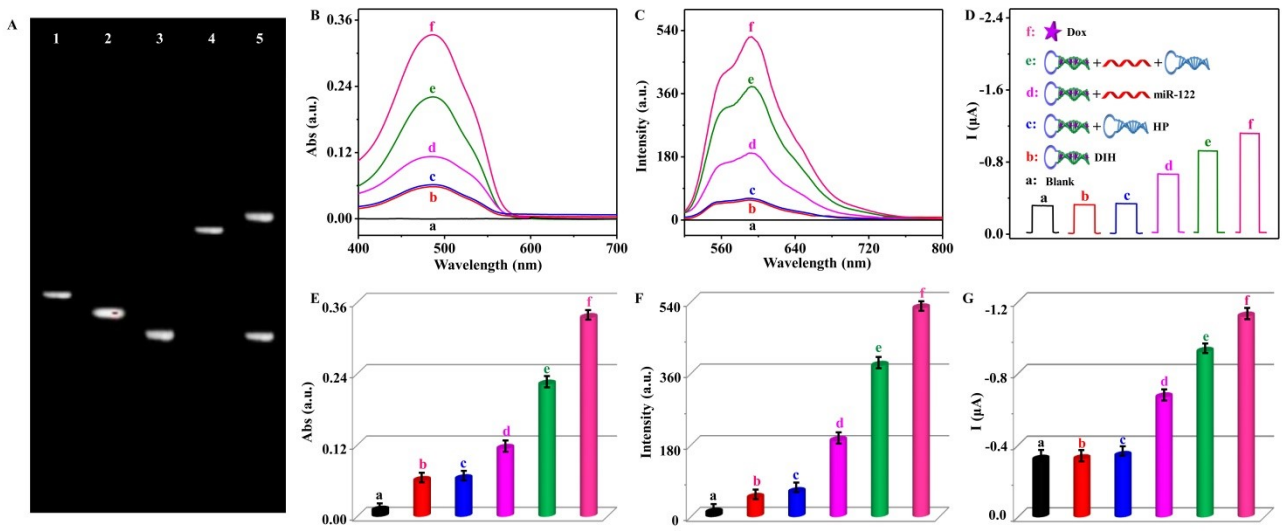

Figure S11 The feasibility of the proposed method for miR-122 detection. (A) PAGE analysis: Lane 1: DIH, lane 2: HP, lane 3: miR-122, lane 4: DIH+miR-122, lane 5: DIH+miR-122+HP. (B) Absorption, (C) Fluorescence, (D) Photocurrent responses and (E, F, G) the corresponding histograms: (a) Blank buffer; (b) DIH; (c) DIH+HP; (d) DIH+miR-122; (e) DIH+miR-122+HP; (f) free Dox. The concentrations of miR-122 and HP were 1.0 nM and 27.0 μM, respectively. The DIH was formed by mixing 60.0 μM of Dox with 20.0 μM of the hairpin probe.

The polyacrylamide gel electrophoresis (PAGE) analysis was performed to verify the strand displacement reaction (SDR) and the feasibility of the sensing platform for miR-122 detection. As shown in Figure S11A, the low molecular weight bands in lanes 1, 2, and 3 correspond to the DIH structure, HP, and miR-122, respectively. When the target miR-122 is present in the reaction system, a large molecular weight product can be observed (lane 4), which is due to the hybridization of DIH and miR-122 to form double-stranded DNA. In comparison with lane 4, two bands appear (lane 5), which is attributed to the hybridization of DIH and HP (the large molecular weight band) that induces SDR and again release miR-122 (the low molecular weight band).

Figure S11B, C, E, and F (curve/panel a) shows absorption and fluorescence spectra of the blank solution, showing no absorption and fluorescence characteristic peaks of Dox. As depicted in curves/panels b, compared to free Dox (curves/panels f), relatively weak absorption and fluorescence intensities are obtained for the DIH structure, probably owing to the fact that the embedded Dox in the duplex DNA has reduced absorption/fluorescence results from self-aggregation and the hydrogen bond formation.[14] Upon addition of the HP to the DIH, changes of the absorption and fluorescence intensities are negligible (curve/panel c) because there is no reaction occurs between the DIH and HP. While increased signals of absorption and fluorescence are observed when incubating the target miR-122 with the DIH structure (curve/panel d) as a result of the binding of miR-122 to the DIH probe opens the hairpin structure, leading to the production of released free Dox in solution with enhanced absorption/fluorescence signals. As shown in curve/panel e, a further enhanced signal is acquired after the co-addition of the HP and miR-122 to

the DIH solution, implying the function of SDR to increase the amount of released free Dox in solution. PEC analysis was then utilized to further validate feasibility of the sensing platforms. For the miR-122 PEC bioassay, compared to the initial photocurrent intensity of the Bi (GLY) modified electrode in blank buffer, a negligible photocurrent change is obtained for that in the presence of the DIH structure or the mixture of the DIH structure and the help DNA (HP) (Figure S11D and G, curves a, b, and c), hinting that there is no direct reaction between the DIH and the HP to induce the release of Dox. Upon the incubation of target miR-122 with its corresponding probe (i.e., the DIH), an increased photocurrent is observed (curve d), which is resulted from the fact that target miR-122 binds to its recognition sequence and directly opens the hairpin structure, leading to the release of free Dox for signal stimuli. As demonstrated in curve e, after the co-addition of target miR-122 and the HP, the increased signal is greater than that merely with target miR-122 without HP (curve d). Clearly, this larger signal increment is caused by the SDR to release increased amount of Dox.

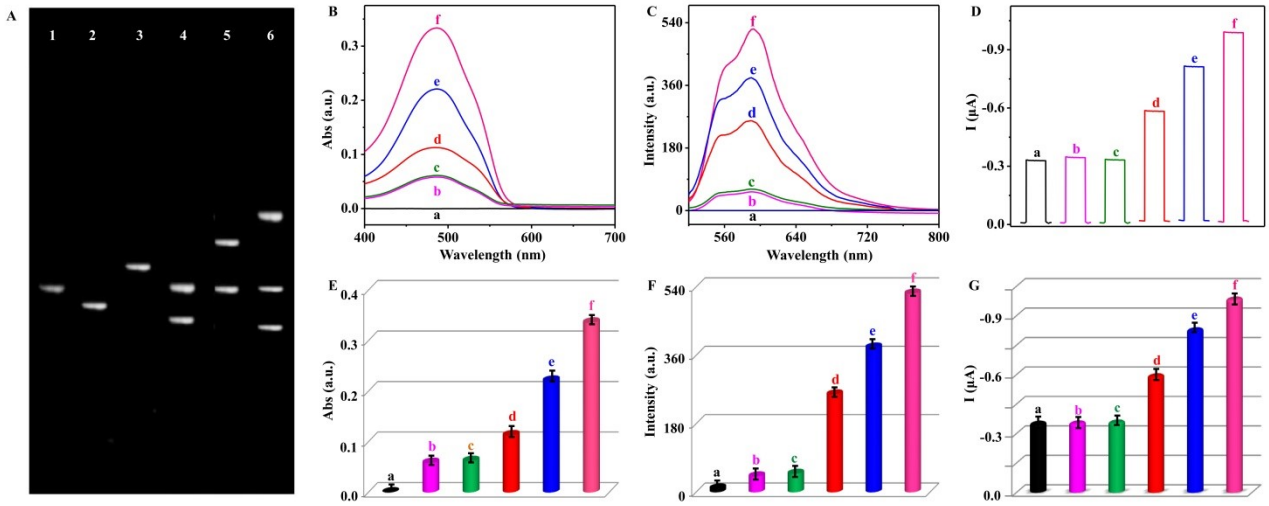

Figure S12. The feasibility of the proposed method for MUC1 protein detection. (A) PAGE analysis: Lane 1: DIH′, lane 2: HP′, lane 3: MUC1 aptamer+auxiliary probe, lane 4: MUC1 aptamer+auxiliary probe+MUC1, lane 5: MUC1 aptamer+auxiliary probe+MUC1+DIH′, lane 6: MUC1 aptamer+auxiliary probe+MUC1+DIH′+HP′. (B) Absorption, (C) Fluorescence, (D) Photocurrent responses and (E, F, G) the corresponding histograms: (a) Blank buffer; (b) DIH′; (c) DIH′+MUC1 aptamer+auxiliary probe+HP′; (d) DIH′+MUC1 aptamer+auxiliary probe+MUC1; (e) DIH′+MUC1 aptamer+auxiliary probe+HP′+MUC1; (f) free Dox. The concentrations of the MUC1 aptamer, auxiliary probe, HP′, and MUC1 were 13.0 μM, 13.0 μM, 20.0 μM and 0.1 ng/mL, respectively. The DIH′ was obtained by mixing 60.0 μM of Dox with 20.0 μM of the corresponding hairpin probe.

As shown in Figure S12A, similarly, the PAGE analysis for MUC1 protein also confirms the occurrence of SDR. For lanes 1 and 2, the bands appearing in the low molecular weight regions are assigned to the DIH' structure and HP', respectively. The slower migrating band (lane 3) is

attributed to the large molecular weight arched structure formed by the hybridization of the MUC1 aptamer and the auxiliary probe. In the presence of the target MUC1 (lane 4), the auxiliary probe is released due to the specific binding of MUC1 to the aptamer, resulting in two low molecular weight bands. In contrast to the two bands (i.e., a large molecular weight double-stranded DNA formed by the hybridization of DIH' and auxiliary probe, and a low molecular weight aptamer probe) in lane 5, there are three bands in lane 6, which are the bands of double-stranded DNA formed by the hybridization of the DIH' structure and HP' (the large molecular weight band), the aptamer and the auxiliary probe (the low molecular weight bands), respectively.

As shown in Figure S12B-G, similar to the results of detecting miR-122, the different signals of absorption, fluorescence, and PEC measurements can also validate feasibility of the strategy for MUC1 protein detection.

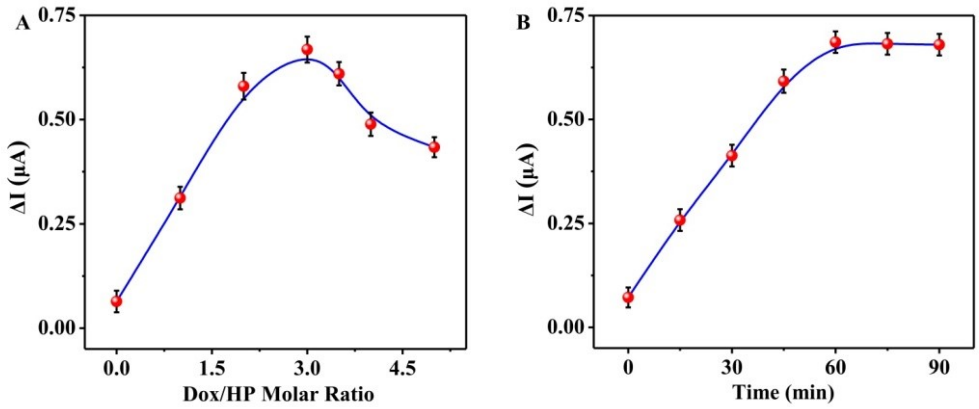

Figure S13. Optimization of (A) the molar ratio of the Dox and the hairpin probe and (B) the reaction time between the miR-122 and the DIH for PEC detection of miR-122.

As shown in Figure S13, the maxima PEC responses of the detection platform for miR-122 are obtained when the molar ratio of Dox to its corresponding hairpin DNA (DIH) is fixed at 3:1 and the reaction time between miR-122 and DIH is selected at 60 min.

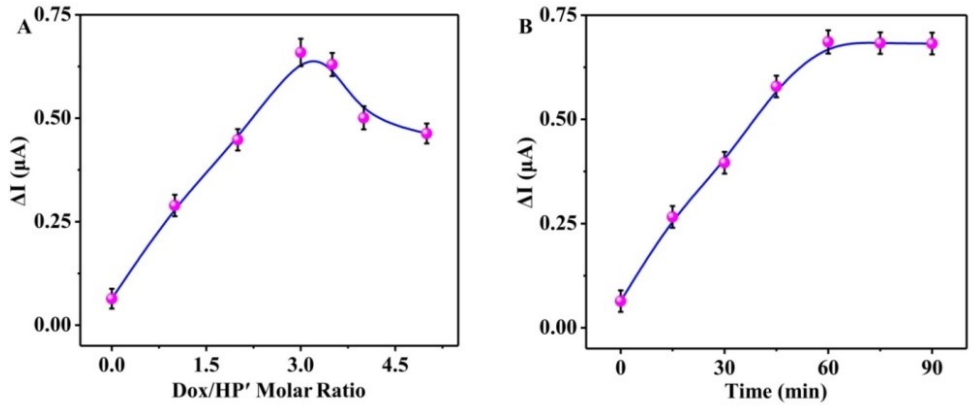

Figure S14. Optimization of (A) the molar ratio of the Dox and the hairpin probe and (B) the reaction time between the auxiliary probe and the DIH′ for PEC detection of MUC1 protein.

As shown in Figure S14, when the molar ratio of Dox to its corresponding hairpin DNA (DIH′) is at 3:1 and the reaction time between the auxiliary probe and DIH′ is chosen at 60 min, the maxima PEC responses of the detection system for MUC1 protein are attained.

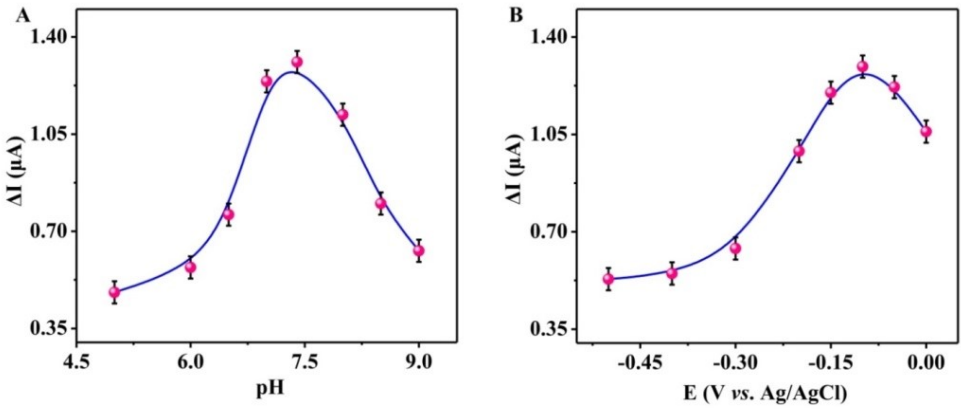

Figure S15. The effect of (A) solution pH and (B) applied potential on the photocurrent responses of the Bi (GLY) electrode to 0.1 mM Dox.

As shown in Figure S15, the optimal pH and applied potential for conducting the PEC measurement in the presence of Dox are summarized as 7.4 and –0.1 V (*vs*. Ag/AgCl), respectively.

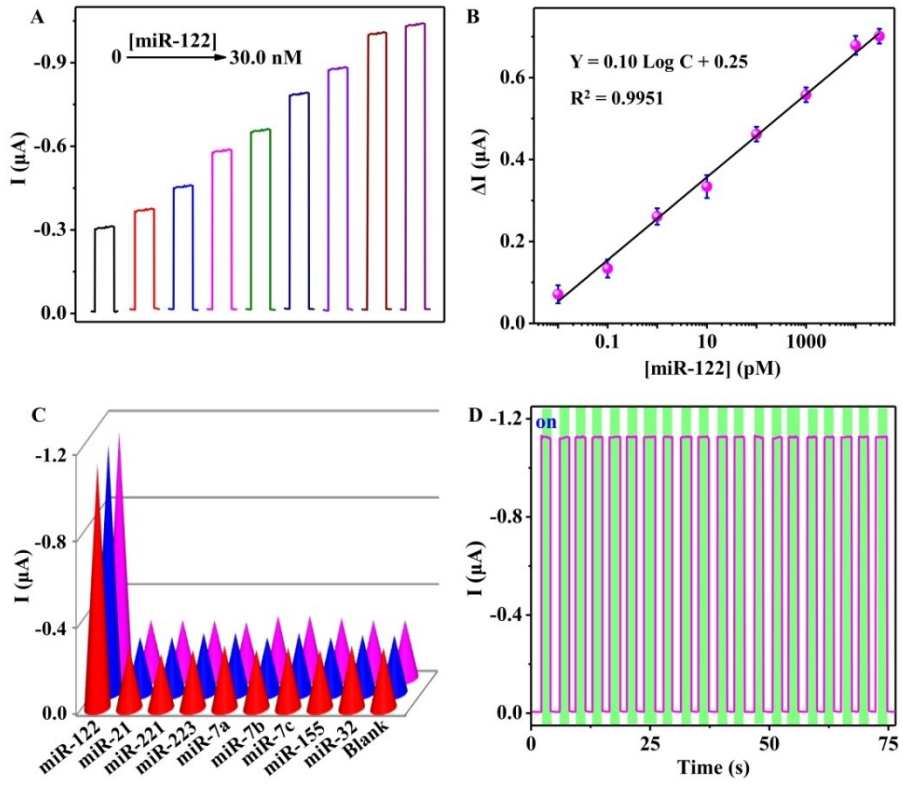

Figure S16. (A) Photocurrent responses of the Bi (GLY) electrode to different concentrations (from left to right, 0, 0.01, 0.1, 1.0, 10.0, 100.0, 1.0×10^3, 1.0×10^4 and 3.0×10^4 pM) of miR-122. (B) The corresponding calibration curve. (C) Selectivity of the miR-122 biosensor. The concentration of miR-122 was 10.0 nM, and the concentration of all other interferents was 500.0 nM. (D) Stability of the biosensor to 3.0×10^4 pM miR-122 by repeated on/off illumination cycles.

The reproducibility of the bioassay was evaluated by assaying 30.0 nM of miR-122 with six independent electrodes under identical conditions, and the relative standard deviation (RSD) was 4.6%, suggesting that the reproducibility of this method was acceptable.

Table S3. Comparison with Different Methods for the Detection of miR-122

Method	Material	Linear range (pM)	LOD (pM)	Reference
SERS*	Ag-HMSs	1.0×10^{-3}–1.0	0.2	15
Fluorometry	TetII	1.0×10^{-2}–1.0×10^{3}	7.2×10^{-3}	16
Fluorometry	FITC	10.0–1.0×10^{4}	8.5	17
Electrochemistry	GO	2.0×10^{-2}–1.0×10^{3}	1.0×10^{-2}	18
Photoelectrochemistry	TiO_2/Au NPs	0.1–3.0×10^{3}	8.3×10^{-2}	19
Photoelectrochemistry	Bi (GLY)	1.0×10^{-2}–3.0×10^{4}	3.2×10^{-3}	This work

*SERS: Surface-enhanced Raman spectroscopy.

Table S4. Comparison with Different Methods for the Detection of MUC1 Protein

Method	Material	Linear range (fg/mL)	LOD (fg/mL)	Reference
Fluorometry	Ag NCs	1.3×10^{6}–2.0×10^{8}	1.8×10^{5}	20
Electrochemistry	ZrHF/mFe_3O_4/mC	1.0×10^{4}–1.0×10^{9}	9.0×10^{2}	21
Electrochemiluminescence	GO–Ag NPs–ABEI	10.0–3.0×10^{7}	2.8	22
Electrochemiluminescence	$CoFe_2O_4$@Au NPs	1.0–1.0×10^{6}	0.6	23
Electrochemiluminescence	ABEI/MIL–101(Fe)	10.0–1.0×10^{7}	1.6	24
Electrochemiluminescence	Au NPs@Fe_3O_4	10.0–1.0×10^{7}	4.5	25
Photoelectrochemistry	Bi (GLY)	1.0–3.0×10^{7}	0.3	This work

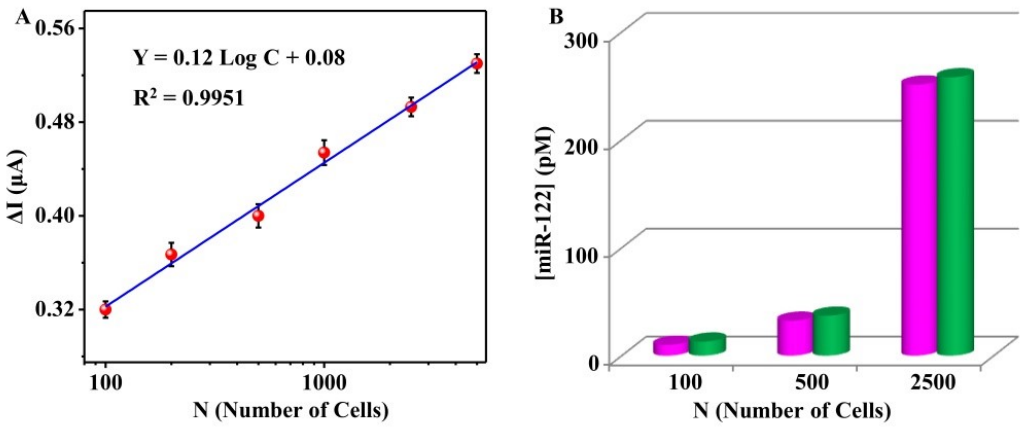

Figure S17. (A) Detection of miR-122 by the proposed PEC assay with different numbers (100, 200, 500, 1000, 2500, and 5000) of MCF-7 cells. (B) Comparison of the responses for miR-122 detection by the proposed PEC assay (rose red bars) and the qRT-PCR method (green bars).

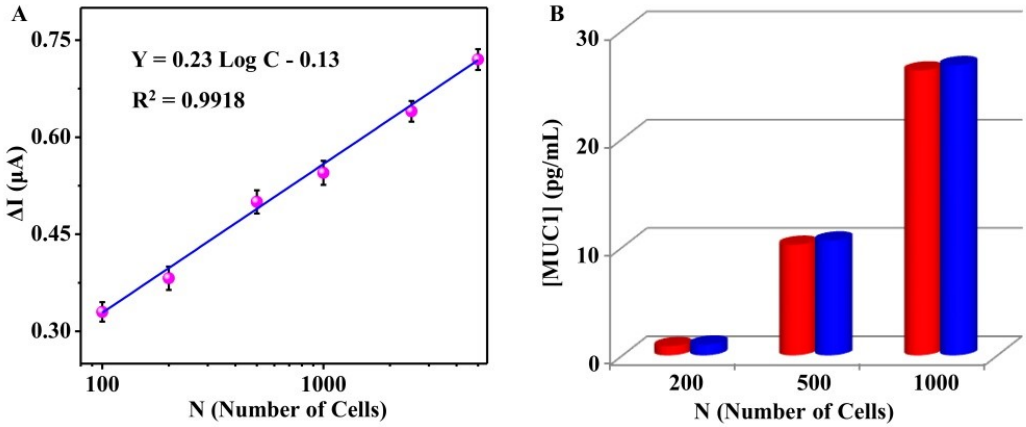

Figure S18. (A) Detection of MUC1 protein by the proposed PEC assay in different numbers (100, 200, 500, 1000, 2500, and 5000) of MCF-7 cells. (B) Comparison of the responses for MUC1 protein detection by the proposed PEC assay (red bars) and the ELISA method (blue bars).

References

1 G. L. Wang, P. P. Yu, J. J. Xu and H. Y. Chen, *J. Phys. Chem. C,* 2009, **113**, 11142–11148.

2 M. S. Wu, D. J. Yuan, J. J. Xu and H. Y. Chen, *Anal. Chem*., 2013, **85**, 11960−11965.

3 Y. M. Nie, X. D. Yuan, P. Zhang, Y. Q. Chai and R. Yuan, *Anal. Chem*., 2019, **91**, 3452−3458.

4 P. Kannan, P. Subramanian, T. Maiyalagan and Z. Q. Jiang, *Anal. Chem*., 2019, **91**, 5824−5833.

5 I. Pastoriza-Santos and L. M. Liz-Marzán, *Adv. Funct. Mater*., 2009, **19**, 679–688.

6 D. Chen, S. E. Pei, Z. S. He, H. B. Shao, J. M. Wang, K. Wang, Y. Wang and Y. X. Jin, *Catalysts,* 2020, **10**, 751–762.

7 R. Mueller, H. K. Kammler, K. Wegner and S. E. Pratsinis, *Langmuir,* 2003, **19**, 160–165.

8 D. Zhao, C. Chen, Y. Wang, H. Ji, W. Ma, L. Zang and J. Zhao, *J. Phys. Chem. C*, 2008, **112**, 5993–6001.

9 J. Lin, W. L. Wang and G. Q. Li, *Adv. Funct. Mater*., 2020, **30**, 2005677.

10 J. B. Gao, J. B. Zhang, J. van de Lagemaat, J. C. Johnson and M. C. Beard, *ACS Nano,* 2014, **8**, 12814–12825.

11 W. Yang, S. Lee, H. J. Kwon, H. Lee, J. Park, Y. Oh, H. Choi and J. Moon, *ACS Nano,* 2018, **12**, 11088−11097.

12 J. Jiang, X. Zhang, P. B. Sun and L. Z. Zhang, *J. Phys. Chem. C,* 2011, **115**, 20555–20564.

13 (a) C. M. R. Wright, K. Ruengkajorn, A. F. R. Kilpatrick, J. C. Buffet and D. O'Hare, *Inorg. Chem*., 2017, **56**, 7842−7850; (b) Y. Liu and P. Y. Zhang, *J. Phys. Chem. C*, 2017, **121**, 23488−23497.

14 X. L. Zhang, X. H. Tan, D. Zhang, N. S. Liao, Y. S. Zheng, A. X. Zheng, Y. Y. Zeng, X. L. Liu and J. F. Liu, *Chem. Commun.,* 2017, **53**, 9979−9982.

15 W. Zhou, Y. F. Tian, B. C. Yin and B. C. Ye, *Anal. Chem*., 2017, **89**, 6120–6128.

16 X. D. Wang, H. Wang, C. H. Liu, H. H. Wang and Z. P. Li, *Chem. Commun.,* 2017, **53**, 1124–1127.

17 Y. C. He, B. C. Yin, L. H. Jiang and B. C. Ye, *Chem. Commun.,* 2014, **50**, 6236–6239.

18 M. X. Liu, S. P. Liang, Y. F. Tang, J. N. Tian, Y. C. Zhao and S. L. Zhao, *Biosens. Bioelectron.,* 2021, **171**, 112676–112681.

19 S. S. Liu, H. J. Cao, X. Y. Wang, W. W. Tu and Z. H. Dai, *Nanoscale,* 2018, **10**, 16474–16478.

20 Y. Y. Wang, S. S. Wang, C. S. Lu and X. M. Yang, *Sens. Actuat. B: Chem.,* 2018, **262**, 9–16.

21 M. H. Wang, B. Hu, H. F. Ji, Y. P. Song, J. M. Liu, D. L. Peng, L. H. He and Z. H. Zhang, *ACS Omega,* 2017, **2**, 6809−6818.

22 X. Y. Jiang, H. J. Wang, H. J. Wang, R. Yuan and Y. Q. Chai, *Anal. Chem*., 2016, **88**,

9243−9250.

23 X. Y. Jiang, H. J. Wang, H. J. Wang, R. Yuan and Y. Q. Chai, *Anal. Chem*., 2017, **89**, 4280−4286.

24 Z. L. Wang, X. Y. Jiang, R. Yuan and Y. Q. Chai, *Biosens. Bioelectron*., 2018, **121**, 250−256.

25 J. X. Wang, Y. Zhuo, Y. Zhou, R. Yuan and Y. Q. Chai, *Biosens. Bioelectron*., 2015, **71**, 407–413.